Approaching isotropic transfer integrals in crystalline organic semiconductors

Qijing Wang,[1,3] Emilio J. Juarez-Perez,[2] Sai Jiang,[1] Mingfei Xiao,[3] Jun Qian,[1] Eun-Sol Shin,[4] Yong-Young Noh,[4] Yabing Qi,[2,*] Yi Shi,[1,†] and Yun Li[1,‡]

[1]*National Laboratory of Solid-State Microstructures, School of Electronic Science and Engineering, Collaborative Innovation Centre of Advanced Microstructures, Nanjing University, Nanjing, 210093, China*

[2]*Energy Materials and Surface Sciences Unit (EMSSU), Okinawa Institute of Science and Technology Graduate University (OIST), 1919-1, Tancha, Onna-son, Kunigami-gun, Okinawa, 904-0495, Japan*

[3]*Optoelectronics Group, Cavendish Laboratory, JJ Thomson Avenue, Cambridge CB3 0HE, United Kingdom*

[4]*Department of Chemical Engineering, Pohang University of Science and Technology, 77 Cheongam-Ro, Nam-Gu, Pohang, 37673, Republic of Korea*

(Received 25 October 2019; revised manuscript received 24 February 2020; accepted 1 April 2020; published 27 April 2020; corrected 26 May 2020)

Dynamic disorders, which possess a finite charge delocalization, play a critical role in the charge transport properties of high-mobility molecular organic semiconductors. The use of two-dimensional (2D) charge transport in crystalline organic semiconductors can effectively facilitate reducing the sensitivity of charge carriers to thermal energetic disorders existing in even single crystals to enhance the carrier mobility. An isotropic transfer integral among adjacent molecules enables a dimensional transition from quasi-one-dimensional to 2D for charge transport among molecules. Herein, a tuned molecular packing, especially molecular rotation, was achieved in highly crystalline organic thin films via a brush-coating method. This tuned molecular packing was favorable for approaching isotropic transfer integrals. Consequently, high-performance organic transistors with a carrier mobility up to 21.5 $cm^2\,V^{-1}\,s^{-1}$ and low angle dependence were obtained. This work presents a unique modulation of molecular packing at the molecular scale to enable less sensitivity of the charge transport to dynamic disorders, providing an alternative route for enhancing the electrical performance of organic electronic devices.

DOI: 10.1103/PhysRevMaterials.4.044604

I. INTRODUCTION

Tremendous effort has been exerted to study the carrier mobility of organic semiconductors, reaching tens of $cm^2\,V^{-1}\,s^{-1}$ within a range that cannot be satisfactorily and separately described by hopping or bandlike transport [1–4]. As described by transient localization theory, the quantum localizations of electronic wave functions at timescales [4,5] are shorter than typical molecular motions and are easily affected by molecular vibrations and the resulting dynamic disorders. A notable strategy to obtain high carrier mobility in crystalline organic semiconductors is to realize high-transfer integrals by increasing the molecular orbital overlapping [4]. Moreover, isotropic two-dimensional (2D) transfer integrals between adjacent molecules can effectively ensure less sensitivity of charge carriers to intrinsic dynamic disorders [6,7], thereby contributing a high overall carrier mobility and low anisotropic discrepancy. From this aspect, tuning orbital overlapping by molecular rotation provides a nonsynthetic technique to adjust the isotropy of transfer integrals in molecular semiconductors [8,9]. Strain in organic semiconductors can efficiently improve the transfer rate along the transport direction by decreasing the π-π stacking distance, whereas the charge transport along other directions contributes little to the whole transfer property [10,11]. Thus far solution processes, such as solution shearing, for organic films have been employed to modulate the molecular packing in and electrical properties of organic crystals with unique polymorphs by narrowing the π-π overlapping in the transport directions [12–16]. However, effectively tuning highly crystalline semiconducting channels to realize isotropic charge transfers remains a great challenge.

Herein, we successfully tuned the molecular packing in highly crystalline molecular dioctylbenzothienobenzothiophene (C_8-BTBT) films in a nonequilibrium state (a unique polymorph) during a solution process. The obtained thin films exhibited single-crystalline properties with distorted molecular packing and molecular rotation. The hole carrier mobility for organic field-effect transistors (OFETs) based on the obtained C_8-BTBT films showed a marked threefold increase, exceeding 20 $cm^2\,V^{-1}\,s^{-1}$, even when compared with that obtained for single-crystal-based devices. We found that the nonequilibrium C_8-BTBT films possess relatively isotropic transfer integrals among adjacent molecules compared with that of single crystals, thereby facilitating the formation of a 2D charge transport. Our results demonstrated the potential of realizing an isotropic charge transfer by molecular rotation as an effective method for developing high-performance OFETs.

*Yabing.Qi@OIST.jp
†yshi@nju.edu.cn
‡yli@nju.edu.cn

II. EXPERIMENT

Substrate preparation. Heavily doped *p*-type silicon wafers with 50-nm-thick thermally grown oxide were used as the substrates. The substrates ($1.5 \times 1.5\,cm^2$) were sequentially cleaned by sonication (100 kHz) in acetone and isopropanol for 8 min each and then treated by UV ozone for 15 min.

Deposition and characterization of C_8-BTBT *films.* The *p*-type organic semiconductor C_8-BTBT (99%) was purchased from Sigma-Aldrich and used without further purification. C_8-BTBT (1.0 wt %) was dissolved in anisole. Chinese brushes (0 G808-8 Martol, China) were purchased from Taobao and sequentially cleaned in acetone and isopropanol. A smooth coating setup was assembled, which includes three stages (Thorlabs, Inc.) to control the position and speed to program the movement of the brush. Three types of writing (using the C_8-BTBT solution as the ink) were used in the experiments, drop casting, bar coating, and microbar coating. A Keyence VHX-5000 digital microscope (Keyence Ltd., Japan) was used to obtain the optical microscopy images of solution-processed C_8-BTBT films. Two types of atomic force microscope (AFM) were performed in this work. For regular AFM, the characterizations were performed on a Veeco MultiMode 8 in tapping mode under ambient conditions. For high-resolution atomic force microscope (HRAFM), the experiments were performed on an Asylum Cypher under ambient conditions using Asylum Arrow UHF AFM tips. Fast Fourier transform (FFT) of AFM data was obtained using IMAGEJ. Transmission electron microsopy (TEM) measurements were carried out by a JEM1230R transmission electron microscope (JEOL), and the evaporated films were directly deposited on carbon-coated Cu grids (#36), and the solution-processed C_8-BTBT films were prepared on mica treated by UV-ozone, which were easy to delaminate for transfer to the carbon-coated Cu grids (#36) [17]. Photoluminescence spectroscopy was acquired using the time-correlated, single-photon counting technique (Hamamatsu, C10627), and excitation was provided by a femtosecond mode-locked Ti:sapphire laser (Spectra-Physics, Mai Tai XF-IMW) at 360 nm with an average power at 8 MHz of 0.74 mW.

Fabrication and electrical measurements of the OFETs. Uniform C_8-BTBT films (trilayers) were selected for better stability to fabricated OFETs. Patterned Au films with a thickness of 100 nm and Au pads with dimensions of $80 \times 120\,\mu m^2$ were thermally evaporated under a deposition rate of $0.1\,Å\,s^{-1}$. The two Au pads were subsequently transferred onto the top of the strained films to form the source and drain electrodes. Electrical measurements were performed using an Agilent B1500 semiconductor parameter analyzer in a closed-cycle cryogenic probe station with a base pressure of $\sim 10^{-5}$ mbar. The saturation region equation [$I_D = \mu_{FET} C_i (W/2L)(V_G - V_{TH})^2$] was applied for calculation of the carrier mobility.

XRD, x-ray reflectivity (XRR), and grazing incidence wide-angle x-ray scattering (GIWAXS) characterizations, and density functional theory (DFT) calculations. The XRD and XRR measurements were carried out in a Bruker D8 Discover instrument (Bruker AXS GmbH, Karlsruhe, Germany) equipped with Cu wavelength $\lambda = 1.54\,Å$ x-ray source operated at 1600 W and Goebel mirror. For XRR, the beam was reduced in the reflectivity plane by a 0.05-mm-wide slit in order to minimize the irradiated footprint at the sample position. After careful alignment of the sample, data were collected from 0° to 10° (2θ) with a 0.01° step. The experimental XRR data were fitted using the GENX v.2.4.10 software [18]. Conventional 2θ-ω scans using Bragg-Brentano configuration were carried out on thin-film samples from 2° to 30° (2θ) with a 0.02° step but using a larger slit (1.2 mm), a fully open detector slit, and a longer accumulation time. The experimental XRD data were fitted using the PROFEX/BGMN v.3.12.0 software [19]. Dimers *AA* and *AB* in strained thin films and single-crystal strained configurations were optimized at the B3LYP/6-311G (*d*, *p*) level using GAUSSIAN 09, REVISION E.01. Charge transport analysis for routes connecting dimers *AA* and *AB* were carried out using MULTIWFN [20]. Charge transfer integrals were calculated using CALC_J, v.1.2 [21]. GIWAXS experiments were performed with an x-ray source (wavelength = 0.138 nm) at the 9A beamline in Pohang Accelerator Laboratory, Korea.

III. RESULTS AND DISCUSSION

A. Crystalline property characterizations and molecular packing of C_8-BTBT films

C_8-BTBT was selected as the organic material for the deposition of single-crystalline semiconducting thin films via the microbar-coating method [Fig. 1(a)] [22,23]. The hair direction was perpendicular to the writing direction, forming an analogous multibar-coating process. The key element in our method was that the solution was shorn by the moving brush and was thus influenced by the hairs through the bar-coating effect, contributing to both straining of the nonequilibrium molecular packing and deforming unit-cell geometries in the C_8-BTBT thin films. At the solution edge retained at the shearing brush, high-rate solvent evaporation occurred due to the high velocity of the solution [inset in Fig. 1(a)], which promoted C_8-BTBT crystallization from a supersaturated zone of the solution. The film property was crucially affected by the number of C_8-BTBT molecules; therefore, the solution concentration was also adjusted to optimize the film morphology (Fig. S1 in the Supplemental Material [24]). The obtained C_8-BTBT films exhibited a layered structure and mainly consisted of bilayer and trilayer films with a large area [Fig. 1(b)]. The single-crystalline feature of the ultrathin C_8-BTBT films was further confirmed via cross-polarized optical microscopy [Figs. 1(c) and 1(d)] to observe the changes in film brightness and color. When the crystal growth direction was parallel or perpendicular to the polarization angle, a completely black image was obtained, indicating that the crystal axes were highly oriented. The C_8-BTBT films exhibited a uniform morphology and atomic smoothness with a root-mean-square roughness of ~0.12 nm [Fig. 1(e)]. The thickness of the step was ~2.95 nm, which was equivalent to the length of one C_8-BTBT molecule [23]. Transmission electron microscopy (TEM) measurements were performed to further evaluate the film crystallinity (Fig. S2 [24]). Clear diffraction patterns were observed, indicating that the films were highly crystalline. Moreover, high-resolution TEM (HRTEM) measurements were conducted to determine

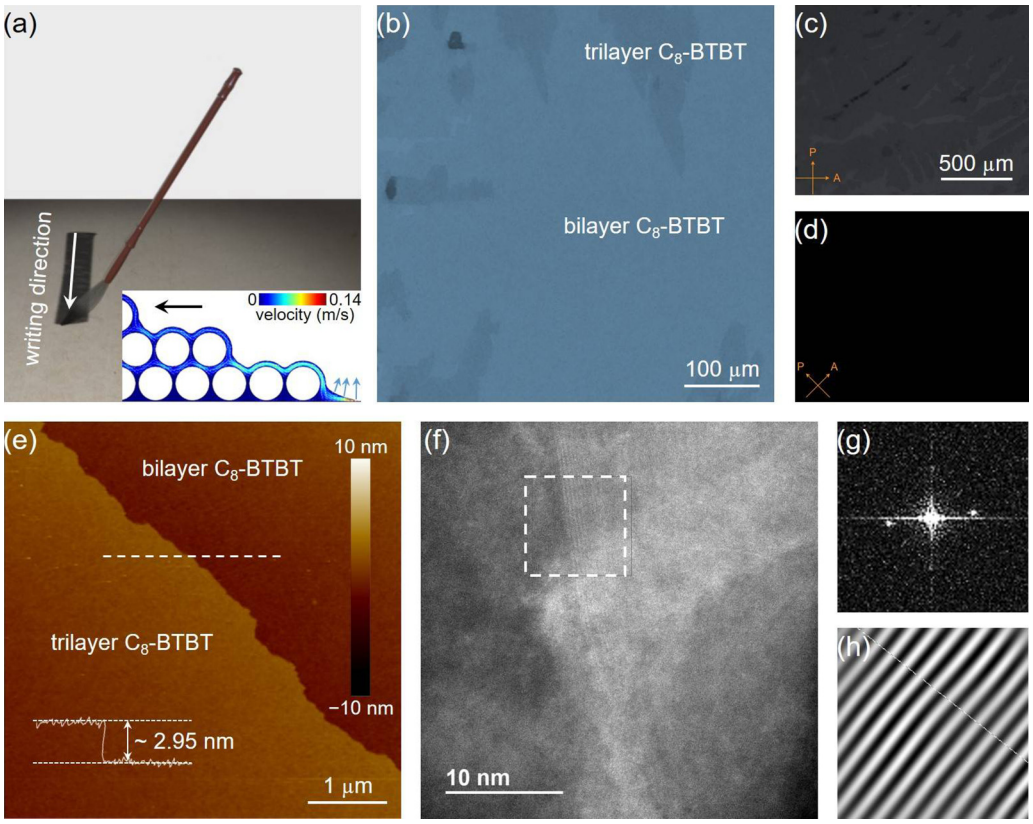

FIG. 1. Crystal property characterizations and molecular packing of the obtained C_8-BTBT films. (a) The illustration of the coating process. The inset is the COMSUL simulation of the microbar-coating method that shows the flow behavior of the solution around the hairs. The color is coded to indicate the scale of velocity. (b) Optical microscope (OM) image of a microbar-coated thin film. (c,d) Cross-polarized OM images of the strained thin films. (e) AFM image of the C_8-BTBT films. (f) HRTEM image of the C_8-BTBT films and (g) its corresponding SAED patterns and (h) filtered IFFT image of the selected area in (f).

the molecular packing in the C_8-BTBT films. As shown in Fig. 1(f), a homogenous morphology for the C_8-BTBT film was observed in the dotted square. The corresponding selected area electron diffraction (SAED) patterns, with clear electron diffraction patterns and the inversion of the filtered fast Fourier transform (IFFT) image of the diffraction patterns, are shown in Figs. 1(g) and 1(h). The patterns presented an intermolecular periodicity within the columns (Fig. S3 [24]) [25]. These results indicated that a highly ordered molecular packing was formed in the obtained C_8-BTBT films.

We assessed the distortion-induced molecular packing of the C_8-BTBT unit cells via x-ray diffraction (XRD) and x-ray reflectivity (XRR) analyses. Typical (00l) diffraction peaks were observed in Fig. 2(a), and the out-of-plane d spacing was 29.065 ± 0.010 Å, which was similar to the layer thickness obtained through AFM. As shown in Fig. 2(b), (00l) fringe peaks parallel and perpendicular to the deposition direction as measured by XRR were observed (Fig. S4 [24]). The small fringes formed due to the underlying native 50-nm-thick SiO_2 substrates. An earlier β parameter was estimated to be 99.4°, which was obtained using the average layer thickness obtained from the XRR model and d spacing obtained from the (00l) diffraction peaks (Table S1 in the Supplemental Material [24]). Notably, this β parameter for the nonequilibrium films was larger than that for the single crystals (92.4°) [23]. The *in*-plane lattice parameters a and b were determined using the FFT transform of the high-resolution AFM (HRAFM) image [Fig. 2(c)]. Highly ordered molecular packing with a typical herringbone-type periodicity was observed. The diffraction spots obtained by the FFT image contained the information needed from the reciprocal lattice upon indexing [Fig. 2(d)]. The values extracted for a and b were 6.354 ± 0.008 Å and 7.856 ± 0.014 Å, respectively (Fig. S5 [24]). Compared with the lattice constants extracted for the C_8-BTBT single crystals (Table S2 [24]), the unit cell in C_8-BTBT films expanded by ∼0.4 Å (or 7.2%) along the a axis, whereas a negligible change was observed along the b axis. In principle, this molecular packing is undesirable because the a axis is the preferred charge transport direction for C_8-BTBT. This distortion-induced enlargement of a can decrease the transfer integral along the a axis. However, the β parameter obtained from the distorted unit cell achieved the opposite value of a bulk crystal. Apart from these characterizations, more details about the molecular packing property for the nonequilibrium C_8-BTBT films were obtained via grazing incidence wide-angle x-ray scattering (GIWAXS) measurements [Fig. 2(e)]. Scattering spots in the out-of-plane directions (q_z) at a given *in*-plane direction (q_{xy}) were observed (Fig. S6 [24]). All structural parameters are summarized in Table I. Thus, the obtained C_8-BTBT films possessed a unique polymorph compared with single crystals. A visual comparison of a single

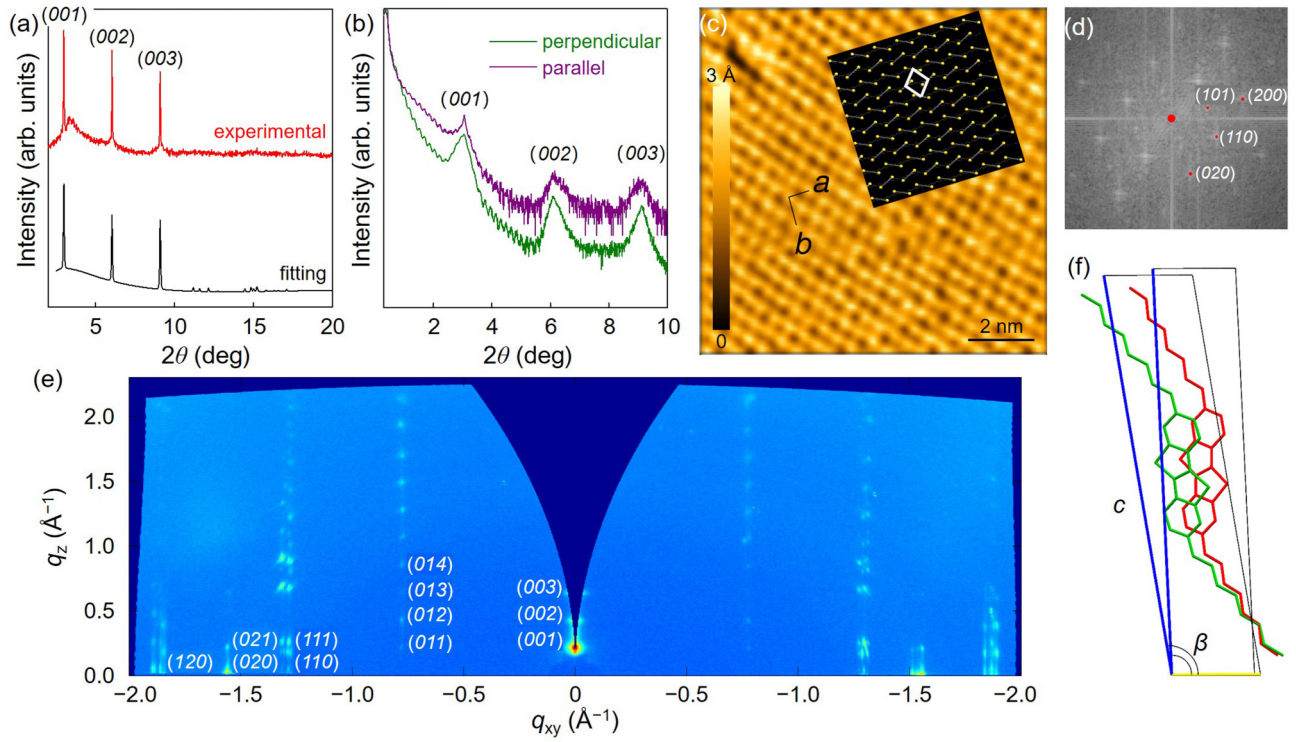

FIG. 2. Crystal property characterizations and molecular packing of the obtained C_8-BTBT films. (a) XRD and (b) XRR patterns characterized along the parallel and perpendicular direction of deposition in microbar-coated films. (c) HRAFM image of the microbar-coated sample. The inset presents the oriented molecular structure according to (d) the FFT image. (e) The GIWAXS patterns of the obtained C_8-BTBT films. (f) Comparison of a single C_8-BTBT molecule in obtained films (green) and single crystals (red).

C_8-BTBT molecule for nonequilibrium films and single crystals is presented in Fig. 2(f).

B. Attaining high-quality nonequilibrium C_8-BTBT films

To evaluate the effect of external factors on the crystalline property, we further deposited the C_8-BTBT films under various processing speeds and solution concentrations. All obtained C_8-BTBT films were measured via GIWAXS (Figs. 3 and S7 [24]). The scattering patterns, especially the (01l) peaks, of the samples deposited at 1, 3, and 5 mm/s (labeled as samples I, II, and III, respectively) exhibited different features. The position of the (01l) plane in the nonequilibrium samples shifted gradually toward that of single-crystal samples with increasing speeds, whereas the scattering property in sample III was almost identical to that in single crystals (Fig. S6 in the Supplemental Material [24]). This processing speed is not the solvent evaporation rate, and generally these two parameters do not match well. Therefore, the tuning effect on molecular packing could not be always sustained, especially during a fast process. Consequently, the C_8-BTBT molecules tended to pack in an equilibrium state. In addition, most (01l) peaks in sample I could be observed, although the intensities of these peaks in sample III was considerably larger, whereas these peaks, except (012), in sample II were missing. The pattern intensity in (12l) tended to decrease with the increase in processing speeds, indicating a weakening molecular packing in these planes. We considered that sample I possessed the highest unit-cell distortion in the unique polymorph. This method was further employed to deposit C_8-BTBT films using a low-concentration solution (0.5 wt %) (Fig. S7 [24]). C_8-BTBT films with a high unit-cell distortion were obtained at a processing speed of 3 mm/s with obvious position shift of the (01l) plane, whereas the 5 mm/s sample possessed a crystal property similar to that of single crystals. Undoubtedly, high processing speed would inevitably result in more structural defects in the stained C_8-BTBT films due to the insufficient time for the molecules to adjust and pack at the proper sites, thereby severely hindering the formation of high-quality distorted C_8-BTBT films in a large scale. Herein, we successfully controlled the C_8-BTBT films with distortion by tuning the processing speed and solution concentration. The molecule number plays a crucial role in molecular packing during crystallization. A balanced relationship between the

TABLE I. Structural parameters characterizing the nonequilibrium C_8-BTBT films and single crystals.

	a (Å)	b (Å)	c (Å)	β (deg)
Nonequilibrium films	6.354 ± 0.008	7.856 ± 0.014	29.065 ± 0.010	99.4 ± 0.01
Single crystal	5.927 ± 0.007	7.88 ± 0.01	29.180 ± 0.004	92.443 ± 0.004

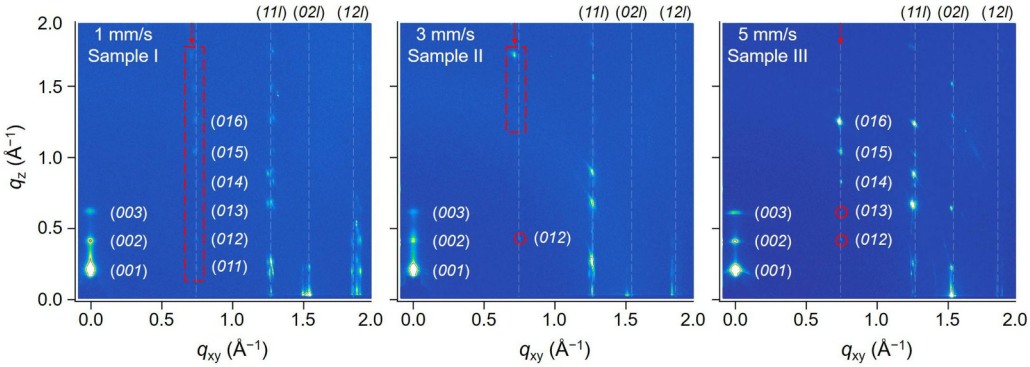

FIG. 3. GIWAXS images of C_8-BTBT films for varying writing speeds. The (*hkl*) indices of (11*l*), (02*l*), and (12*l*) are shown on the top. The dashed lines represent the positions of scattering patterns of C_8-BTBT single crystals. The shift of red arrows on the (01*l*) plane corresponding to the dashed line suggest the unit-cell distortion of C_8-BTBT molecular packing. The number of scattering patterns in the (01*l*) plane and the corresponding intensity also indicate the packing property along with the increasing speeds. Small shifts of (02*l*) and (12*l*) are observed in the sample deposited at 3 mm/s.

number of C_8-BTBT molecules and processing speed effectively regulates the external mechanical force on molecular packing and the corresponding crystalline property. As a result, a C_8-BTBT concentration of 1.0 wt % and an operation speed of 1 mm/s were utilized to deposit high-quality nonequilibrium films.

C. Charge transport in the nonequilibrium C_8-BTBT films

The charge transport among adjacent C_8-BTBT molecules in herringbone-type molecular packing was investigated using the two distinct molecular pairs observed along the intra- and intercolumnar directions, labeled as dimers *AA* and *AB*, respectively [Fig. 4(a)]. We compared the charge transport between these dimers obtained from the single-crystal structure and the dimers *AA* and *AB* from the nonequilibrium C_8-BTBT films. Four outer carbon atoms (two for each monomer as indicated by the blue spheres in Fig. S8 [24]) not involved in the HOMO or LUMO of C_8-BTBT films were selected to constrain in space both polymorphs in a simplified model structure of C_8-BTBT. With the exception of these four carbon atoms, all remaining atoms in the dimer assemble were relaxed via density functional theory (DFT) methods. Upon optimization of the dimers *AA* and *AB* in single-crystal and unique polymorph structures, we employed Yoshizawa's indices at the atomic scale obtained from the DFT calculations to compare the transport properties between adjacent C_8-BTBT molecules in the nonequilibrium films and single crystals [26–29]. Charge carriers normally transport through the π-π overlapping area (thiophene heterocycles) in C_8-BTBT molecules; the best charge transport routes ranked by transmission probability are shown in Fig. 4(b). These routes involved mostly frontier orbitals associated with sulfur (S) and carbon (C) atoms adjacent to S in the C_8-BTBT dimers. The analysis of the charge transport route is presented in Fig. 4(c) and Table S3 in the Supplemental Material [24]. G_{ij} quantifies the transmission probability between two atom sites. Negligible differences in G_{ij} were observed in dimer *AA* (*a* axis) in the nonequilibrium films and single crystals. Notably, the values for G_{ij} of the four routes in dimer *AB* (*ab* plane) in distorted films were markedly enhanced compared with those in single crystals.

Furthermore, charge transport in organic semiconductors at the molecular scale is mainly determined by the transfer integrals (*J*) and their isotropy in the *in*-plane pathways. The DFT calculations for charge transfer were also performed to investigate the transfer integrals and charge transport. The transfer integrals of hole and electron in the directions of dimers *AA* and *AB* of nonequilibrium films and single crystals are presented in Fig. 4(d) and Table S4 [24]. J_{AA} slightly decreased from 25.3 meV in single crystals to 21.9 meV in the distorted C_8-BTBT films, whereas J_{AB} markedly increased from 0.1 to 11.0 meV. This result was in good agreement

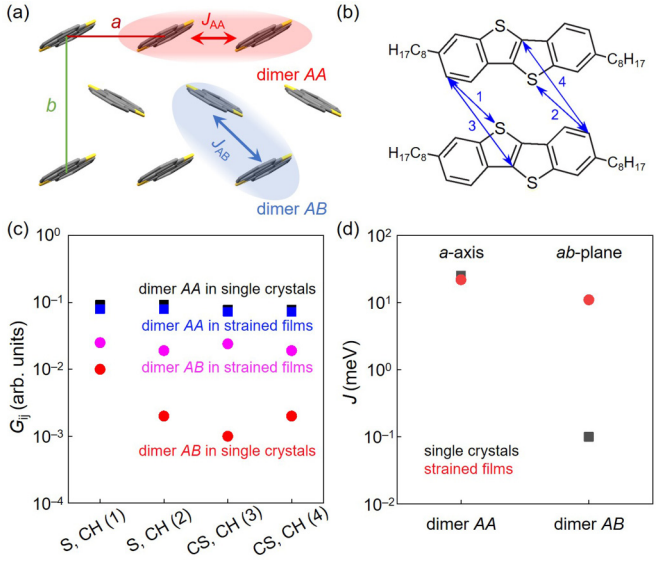

FIG. 4. Charge transport properties from DFT calculations. (a) Top view projection along the *c* axis showing dimers *AA* and *AB* in the crystal structure of C_8-BTBT. (b) Schematic illustration depicting the largest four charge transport routes between C_8-BTBT molecules. (c) Charge transport route analysis of both dimers *AA* and *AB* in the nonequilibrium films and single crystals. (d) Calculated *J* in the *a* axis and *ab* plane.

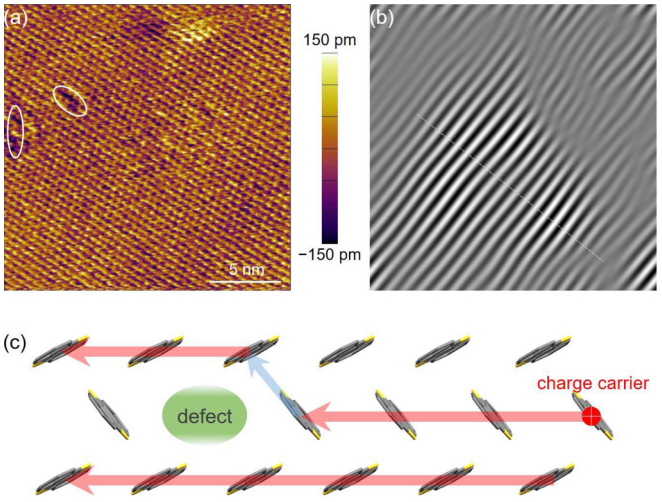

FIG. 5. Structural defects and disorders in the nonequilibrium C_8-BTBT films. (a) HRAFM image of microbar-coated C_8-BTBT films. Some mismatches and defects can be observed (white circles). (b) Filtered IFFT image of the selected area in Fig. 1(f), showing the intermolecular periodicity within the columns. Some fuzzy distorted areas are easily observed, indicating the existence of defects and lattice mismatch in the C_8-BTBT films. (c) Schematic of charge transfer showing the effective charge transport formed by virtue of the in-plane 2D pathways when the hole carriers encounter structural defects or thermal disorders in the obtained C_8-BTBT films.

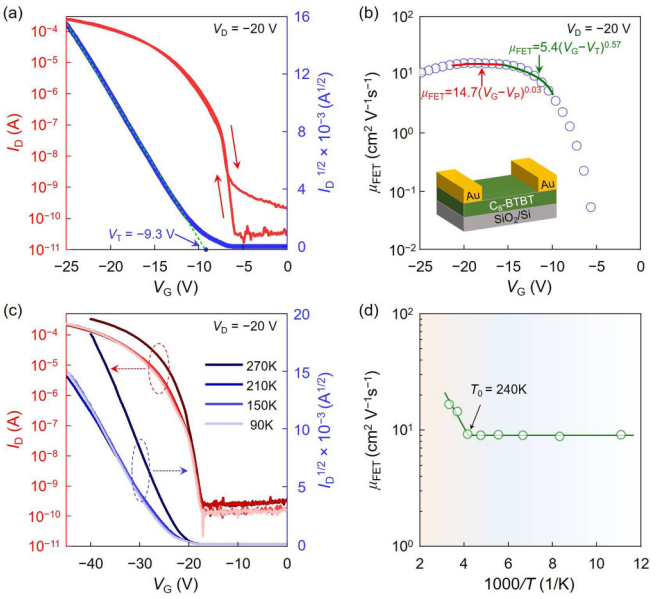

FIG. 6. Electrical characterizations of OFETs based on distorted C_8-BTBT films. (a) Transfer characteristics measured in the saturation regime ($V_D = -20$ V). The channel width and length are 80 and 40 μm, respectively. (b) Gate-voltage dependence of the carrier mobility in the C_8-BTBT transistors. The inset shows a schematic illustration of a bottom-gate top-contact transistor. (c) I_D and $I_D^{1/2}$ measured in the saturation regime ($V_D = -20$ V) under various temperatures. (d) Temperature dependence of μ_{FET} calculated from the transfer curves.

with the analysis of the electron transmission routes at the atomic scale. In the distorted C_8-BTBT films, a relatively balanced charge transfer in the *a* axis and *ab* plane facilitated efficient 2D transport, whereas the hole transport in the single crystals was fundamentally produced along the *a* axis directions and almost negligible along the *ab* plane directions (or 1D transport). In the single crystals, charge carriers were easily impeded by the existing defects and disorders, resulting in a low transfer efficiency [Figs. 5(a) and 5(b)]. In the distorted films, these typical *in*-plane 2D pathways offered an alternative route for charge carriers when encountering energetic disorders and structural defects, leading to a more efficient charge transport, thereby resulting in better device performance [Fig. 5(c)]. This result was also supported by simplified electrical circuit simulation that the 2D circuit facilitated to obtain high currents (Fig. S9 [24]).

D. Electrical performance for the C_8-BTBT OFETs

To evaluate the electrical property of the obtained films, we fabricated planar OFETs using the nonequilibrium C_8-BTBT films. Figure 6(a) shows the typical transfer characteristics of the C_8-BTBT OFETs, yielding a high carrier mobility (μ_{FET}) of 16.0 cm^2 V^{-1} s^{-1}, which was higher than that obtained using single-crystal-based devices (4.9 cm^2 V^{-1} s^{-1}). This device also exhibited a high on/off ratio of $\sim 10^6$ and a low subthreshold swing (*SS*) of 391 mV decade^{-1}. The maximum mobility reached as high as 21.5 cm^2 V^{-1} s^{-1}. The average carrier mobility reached 15.6 ± 2.7 cm^2 V^{-1} s^{-1} (Fig. S10 [24]), which was threefold higher than that obtained for single-crystal-based devices (5.1 ± 1.2 cm^2 V^{-1} s^{-1}).

Considering the markedly enhanced device performance of the obtained C_8-BTBT OFETs, we investigated further the properties of the obtained films to understand this result. First, distortion (or strain) in organic molecular crystals may influence the energy level of the semiconductors. Thus, ultraviolet photoelectron spectroscopy measurements were performed to investigate the energy levels of the C_8-BTBT films; no obvious difference was observed (Fig. S11 [24]). Second, trap density of states (DOS), which is related to multiple trapping and release [30,31] and efficiency of the charge transport mechanism [32], have a remarkable influence on device performance. Thus, we estimated the maximum density of the interfacial traps (N_{trap}) resulting from the dielectric property and defects at the semiconductor/dielectric interface. The N_{trap} value for the 2D C_8-BTBT devices was $\sim 2.41 \times 10^{12}$ eV^{-1} cm^{-2}; this value was slightly lower than that obtained for the single-crystal devices ($\sim 2.45 \times 10^{12}$ eV^{-1} cm^{-2}). The trap states of both samples were further characterized by photoluminescence spectroscopy (Fig. S12 [24]) [33]. The extracted decay time for the strained samples and single crystals was 1.06 ± 0.02 and 0.85 ± 0.02 ns, respectively, indicating a slightly lower DOS in the brush-coated films. Compared with the substantially increased μ_{FET}, the negligible reduction in trap density was not considered as the main contributor to the performance enhancement for the OFET devices.

In addition, μ_{FET} rapidly increased and eventually reached a plateau as the carrier density gradually increased along with the increasing gate voltage [Fig. 6(b)], indicating the

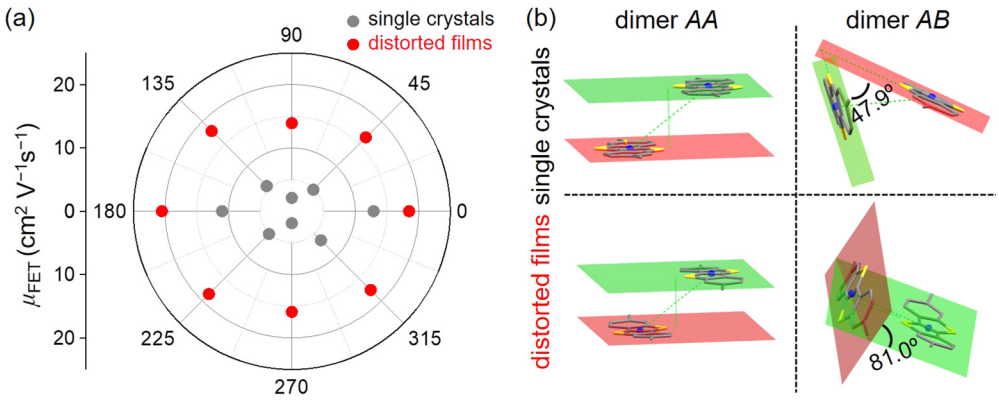

FIG. 7. (a) Carrier mobility of OFETs based on distorted C_8-BTBT films as a function of angle between channel and the deposition direction. (b) Distortion-induced molecular rotation. C_8-BTBT molecular packing in dimers *AA* and *AB* in single crystals and unique polymorphic films, showing the relative molecular rotation in dimers.

formation of a high-quality C_8-BTBT film [34]. Then, μ_{FET} slightly decreased because of the scattering effects, such as electron-electron interactions. We further fitted the V_G-μ_{FET} dependence by the power-law equation ($\mu_{FET} = K[V_G\text{-}V_{T,P}]^{\gamma}$). A transition of charge transport from trap-limited conduction ($\gamma = 0.57$) to percolation conduction ($\gamma = 0.03$) was observed [Fig. 6(b)] [35,36].

To examine the charge transport behavior in distorted C_8-BTBT OFETs, we further characterized the transfer curves under different temperatures. As shown in Fig. 6(c), the I_D and $I_D^{1/2}$ curves remained approximately unchanged when the temperature decreased to below 240 K. The value of calculated carrier mobility exhibited two typical feathers within the temperature range of 300–240 K (range I) and 240–90 K (range II) [Fig. 6(d)]. In range I, μ_{FET} decreased from $\sim$16.0 cm^2 V^{-1} s^{-1} at 300 K to $\sim$9 cm^2 V^{-1} s^{-1} at 240 K along with decreasing temperature, whereas μ_{FET} became temperature independent in range II. This behavior was somewhat unexpected in normal organic semiconductors, which mostly exhibit hopping or bandlike charge transport. This behavior, which has been checked in ten distorted film-based samples, was somewhat unexpected in normal organic semiconductors, which mostly exhibit hopping or bandlike charge transport. This phenomenon is not yet fully understood. A possible explanation is that the charge transport is governed by trap-limited conduction (300–240 K) and percolation conduction (240–90 K), respectively [35,36]. Another explanation is the glasslike transition at a typical temperature (240 K for C_8-BTBT), which could induce the freezing-in of orientational disorders in organic molecules [37]. Furthermore, this phenomenon could also be a result of the competition between hopping and bandlike transport. This temperature-independent charge transport was also observed in other high-performance OFETs, and the intrinsic mechanism behind this phenomenon should be further investigated [38,39].

E. Isotropic property of the carrier mobility

The angle dependence of μ_{FET} and deposition direction were examined to determine the advantage of 2D charge transfer in OFETs [Fig. 7(a)]. The devices based on unique polymorphic C_8-BTBT films exhibited lower angle-dependent discrepancy compared with that based on equilibrium samples (Fig. S13 in the Supplemental Material [24]). This feather was attributed to the *in*-plane 2D pathway formed because of the close transfer integrals in the *a* axis and *ab* plane. In consideration of the negative effect of an enlarged *a* parameter in charge transport, another crucial lattice parameter, β, which is influenced by the nonequilibrium state and affects the overall charge transport, should be examined. Distortion in organic materials at the molecular scale not only features in the molecular packing distance but also in the relative molecular rotation among adjacent molecules in dimer *AB*. Based on the DFT calculations, the markedly increasing J_{AB} possibly originated from the molecular rotation induced by the lattice distortion. Figure 7(b) clearly illustrates the molecular rotation of both dimers in nonequilibrium films and single crystals as obtained after DFT structure optimization. We found that the angle between molecules in dimer *AB* in nonequilibrium films was considerably larger than that in single crystals, increasing from 47.9° to 81.0° and thus forming a *T*-shape structure via such a molecular rotation (Table II) [8,9]. Hence, the improved isotropic transfer integrals of the distorted C_8-BTBT films were attributed to the molecular rotation. Notably, the minute variation in molecular packing distance and enlarged β parameter facilitated a molecular

TABLE II. The extracted molecular packing for dimers *AA* and *AB* in the nonequilibrium films and single crystals.

	Dimer *AA*		Dimer *AB*	
	Distance (Å)	Rotation angle (deg)	Distance (Å)	Rotation angle (deg)
Nonequilibrium films	6.276	0.001	5.823	81.0
Single crystals	5.995	0	5.378	47.9

rotation in dimer *AB* and significantly affected the transport properties of the distorted films. This technique is applicable to a broad class of functional soluble organic semiconductors with a herringbone-type molecular packing feature. We attributed this change in molecular rotation to the existence of microstructures at the brush surface. For comparison, traditional bar coating was utilized to deposit the C_8-BTBT films under the same condition (Fig. S14 [24]). However, based on the XRD, XRR, and HRAFM data, and DFT calculations, no such molecular rotation occurred.

IV. CONCLUSIONS

In this work, we successfully tuned the transfer integrals in the *a* axis and *ab* plane to realize an isotropic charge transport via molecular rotation in nonequilibrium crystalline C_8-BTBT films. This molecular rotation greatly enhanced the charge transfer among intercolumnar molecules, regardless of the decrease in intracolumnar molecules. As expected, the carrier mobility of nonequilibrium C_8-BTBT film-based OFETs yielded average and maximum values of 15.6 ± 2.7 and $21.5\,cm^2\,V^{-1}\,s^{-1}$, respectively. The carrier mobility exhibited a low anisotropic discrepancy compared with that of equilibrium samples. Conclusively, the charge transfer in dimer *AA* dramatically increased in these nonequilibrium C_8-BTBT films, whereas that in dimer *AB* slightly decreased due to the molecular rotation, leading to the transition in charge transfer from quasi-1D transport in single crystals to 2D in the unique polymorphic films. The 2D charge transport enables a more efficient pathway for charge carriers in distorted films and is less sensitive to dynamic disorders and structural defects. Our work presents a strategy for tuning the molecular packing and realizing an isotropic charge transport in organic molecular semiconductors.

ACKNOWLEDGMENTS

This work was supported by China Postdoctoral Innovation Program, China Postdoctoral Science Foundation under Grant No. 2019M651782, NSFJS under Grant No. BK20170075, and NSFC under Grants No. 61774080 and No. 51861145202.

Q.W. and E.J.J.-P. contributed equally to this work.

[1] Y. C. Cheng, R. J. Silbey, D. A. Da Silva Filho, J. P. Calbert, J. Cornil, and J. L. Brédas, J. Chem. Phys. **118**, 3764 (2003).
[2] S. Ciuchi and S. Fratini, Phys. Rev. Lett. **106**, 166403 (2011).
[3] S. Ciuchi, R. C. Hatch, H. Höchst, C. Faber, X. Blase, and S. Fratini, Phys. Rev. Lett. **108**, 256401 (2012).
[4] S. Fratini, D. Mayou, and S. Ciuchi, Adv. Funct. Mater. **26**, 2292 (2016).
[5] D. P. McMahon and A. Troisi, ChemPhysChem **11**, 2067 (2010).
[6] S. Fratini, S. Ciuchi, D. Mayou, G. T. De Laissardière, and A. Troisi, Nat. Mater. **16**, 998 (2017).
[7] S. Illig, A. S. Eggeman, A. Troisi, L. Jiang, C. Warwick, M. Nikolka, G. Schweicher, S. G. Yeates, Y. Henri Geerts, J. E. Anthony, and H. Sirringhaus, Nat. Commun. **7**, 10736 (2016).
[8] S. Tsuzuki, K. Honda, and R. Azumi, J. Am. Chem. Soc. **124**, 12200 (2002).
[9] R. G. Huber, M. A. Margreiter, J. E. Fuchs, S. Von Grafenstein, C. S. Tautermann, K. R. Liedl, and T. Fox, J. Chem. Inf. Model. **54**, 1371 (2014).
[10] G. Giri, E. Verploegen, S. C. B. Mannsfeld, S. Atahan-Evrenk, D. H. Kim, S. Y. Lee, H. A. Becerril, A. Aspuru-Guzik, M. F. Toney, and Z. Bao, Nature **480**, 504 (2011).
[11] G. Giri, R. Li, D. M. Smilgies, E. Q. Li, Y. Diao, K. M. Lenn, M. Chiu, D. W. Lin, R. Allen, J. Reinspach, S. C. B. Mannsfeld, S. T. Thoroddsen, P. Clancy, Z. Bao, and A. Amassian, Nat. Commun. **5**, 3573 (2014).
[12] Y. Yuan, G. Giri, A. L. Ayzner, A. P. Zoombelt, S. C. B. Mannsfeld, J. Chen, D. Nordlund, M. F. Toney, J. Huang, and Z. Bao, Nat. Commun. **5**, 3005 (2014).
[13] F. Molina-Lopez, H. Yan, X. Gu, Y. Kim, M. F. Toney, and Z. Bao, Adv. Funct. Mater. **27**, 1605503 (2017).
[14] M. W. Kim, S. Kwon, J. Kim, C. Lee, I. Park, J. H. Shim, I. S. Jeong, Y. R. Jo, B. Park, J. H. Lee, K. Lee, and B. J. Kim, Small **16**, 1906109 (2019).
[15] Z. Zhang, B. Peng, X. Ji, K. Pei, and P. K. L. Chan, Adv. Funct. Mater. **27**, 1703443 (2017).
[16] S. Paek, P. Schouwink, E. N. Athanasopoulou, K. T. Cho, G. Grancini, Y. Lee, Y. Zhang, F. Stellacci, M. K. Nazeeruddin, and P. Gao, Chem. Mater. **29**, 3490 (2017).
[17] Q. Wang, E. J. Juarez-Perez, S. Jiang, L. Qiu, L. K. Ono, T. Sasaki, X. Wang, Y. Shi, Y. Zheng, Y. Qi, and Y. Li, J. Phys. Chem. Lett. **9**, 1318 (2018).
[18] M. Björck and G. Andersson, J. Appl. Crystallogr. **40**, 1174 (2007); also see http://genx.sf.net.
[19] N. Doebelin and R. Kleeberg, J. Appl. Crystallogr. **48**, 1573 (2015); also see http://profex.doebelin.org/.
[20] T. Lu and F. Chen, J. Comput. Chem. **33**, 580 (2012).
[21] https://github.com/JoshuaSBrown/QC_Tools.
[22] H. Minemawari, T. Yamada, H. Matsui, J. Y. Tsutsumi, S. Haas, R. Chiba, R. Kumai, and T. Hasegawa, Nature **475**, 364 (2011).
[23] T. Izawa, E. Miyazaki, and K. Takimiya, Adv. Mater. **20**, 3388 (2008).
[24] See Supplemental Material at http://link.aps.org/supplemental/10.1103/PhysRevMaterials.4.044604 for supplementary figures and tables of OM, TEM, GIWAXS, UPS, and PL characterizations, and electrical characterizations.
[25] W. Pisula, A. Menon, M. Stepputat, I. Lieberwirth, U. Kolb, A. Tracz, H. Sirringhaus, T. Pakula, and K. Müllen, Adv. Mater. **17**, 684 (2005).
[26] K. Yoshizawa, Acc. Chem. Res. **45**, 1612 (2012).
[27] A. Troisi, J. Chem. Phys. **134**, 034702 (2011).
[28] D. Niedzialek, I. Duchemin, T. B. De Queiroz, S. Osella, A. Rao, R. Friend, X. Blase, S. Kümmel, and D. Beljonne, Adv. Funct. Mater. **25**, 1972 (2015).
[29] X. Xie, A. Santana-Bonilla, and A. Troisi, J. Chem. Theory Comput. **14**, 3752 (2018).
[30] G. Horowitz, Adv. Mater. **10**, 365 (1998).
[31] D. Braga and G. Horowitz, Adv. Mater. **21**, 1473 (2009).
[32] W. L. Kalb and B. Batlogg, Phys. Rev. B **81**, 035327 (2010).

[33] D. Shi, V. Adinolfi, R. Comin, M. Yuan, E. Alarousu, A. Buin, Y. Chen, S. Hoogland, A. Rothenberger, K. Katsiev, Y. Losovyj, X. Zhang, P. A. Dowben, O. F. Mohammed, E. H. Sargent, and O. M. Bakr, Science **347**, 519 (2015).

[34] Q. Wang, S. Jiang, L. Qiu, J. Qian, L. K. Ono, M. R. Leyden, X. Wang, Y. Shi, Y. Zheng, Y. Qi, and Y. Li, ACS Appl. Mater. Inter. **10**, 22513 (2018).

[35] S. Lee, K. Ghaffarzadeh, A. Nathan, J. Robertson, S. Jeon, C. Kim, I. H. Song, and U. I. Chung, Appl. Phys. Lett. **98**, 203508 (2011).

[36] H. Faber, S. Das, Y.-H. Lin, N. Pliatsikas, K. Zhao, T. Kehagias, G. Dimitrakopulos, A. Amassian, P. A. Patsalas, and T. D. Anthopoulos, Sci. Adv. **3**, e1602640 (2017).

[37] K. P. Goetz, A. Fonari, D. Vermeulen, P. Hu, H. Jiang, P. J. Diemer, J. W. Ward, M. E. Payne, C. S. Day, C. Kloc, V. Coropceanu, L. E. McNeil, and O. D. Jurchescu, Nat. Commun. **5**, 5642 (2014).

[38] W. Xie, K. Willa, Y. Wu, R. Häusermann, K. Takimiya, B. Batlogg, and C. D. Frisbie, Adv. Mater. **25**, 3478 (2013).

[39] M.-J. Sher, J. A. Bartelt, T. M. Burke, A. Salleo, M. D. McGehee, and A. M. Lindenberg, Adv. Electron. Mater. **2**, 1500351 (2016).

Correction: The given name of the sixth author contained a typographical error and has been fixed.